Stanford Exploration Project, Report 124, April 4, 2006, pages 9–24

Wave-equation angle-domain common-image gathers for converted waves: Part 2

Daniel A. Rosales, Sergey Fomel, Biondo L. Biondi, and Paul C. Sava

ABSTRACT

Common-image gathers are very useful for velocity and amplitude analysis. Wavefield-extrapolation methods produce Angle-Domain Common-Image Gathers (ADCIGs). For the conventional PP case, ADCIGs are a function of the opening angle. However, the ADCIGs for converted-wave data (PS-ADCIGs) are a function of the half-aperture angle, that is, the incidence angle plus the reflection angle. In PS-ADCIGs, both the P-to-S velocity ratio (γ) and the image dip play a major role in transforming the subsurface offset into the opening angle. We introduce a simple methodology to compute PS-ADCIGs. Our methodology exploits the robustness of computing PP-ADCIGs, and incorporates the velocity ratio (γ), with an image dip field, which is estimated along the prestack image. Our methodology also transforms the half-aperture angle in PS-ADCIGs into an independent P-incidence angle to form P-ADCIGs, and an independent S-reflection angle to form S-ADCIGs. Numerical studies show that when the P-to-S velocity ratio and image midpoint information are not incorporated, the error in computing PS-ADCIGs is large enough to introduce artifacts in the velocity model. Synthetic results show the accuracy of the transformation introduced in this paper. Real data results on the 2-D Mahogany field show the practical application and implications for converted-wave angle-domain common-image gathers.

INTRODUCTION

Imaging is the combined process of migration and velocity analysis. The final image provides two important pieces of information about the earth's subsurface: its structure and some of its rock properties. To obtain a reliable image, we need a reliable velocity model. Therefore, the imaging process becomes a combined procedure between migration and migration velocity analysis.

The final image by itself provides information about the accuracy of the velocity model. This information is present in the redundancy of the prestack seismic image, (i.e. non-zero-offset images). For 2-D seismic data, the information is distributed along a 3-dimensional image space, the coordinates of which are $I(\mathbf{m}_\xi = (m_\xi, z_\xi), h)$. The subsets of this image for a

fixed image point (m_ξ) with coordinates (z_ξ,h) are known as common-image gathers (CIGs), or common-reflection-point gathers (CRPs). If the CIGs are a function of (z_ξ,h), the gathers are also referred as offset-domain common-image gathers (ODCIGs). These gathers can also be expressed in terms of the opening angle θ, by transforming the offset axis (h) into the opening angle (θ) to obtain a common-image gather with coordinates (z_ξ,θ); these gathers are known as Angle-Domain Common-Image Gathers (ADCIGs) (de Bruin et al., 1990; Prucha et al., 1999; Brandsberg-Dahl et al., 1999; Rickett and Sava, 2002; Sava and Fomel, 2003; Biondi and Symes, 2004).

There are two kinds of ODCIGs: those produced by Kirchhoff migration, and those produced by wavefield-extrapolation migration, referred to, from now on, as wave-equation migration. There is a conceptual difference in the offset dimension between these two kinds of gathers. For Kirchhoff ODCIGs, the offset is a data parameter ($h = h_D$), and involves the concept of flat gathers. For wave-equation ODCIGs, the offset dimension is a model parameter ($h = h_\xi$), and involves the concept of focused events. In this paper, we will refer to these gathers as subsurface offset-domain common-image gathers (SODCIGs).

There are problems observed with ODCIGs, which can be alleviated by parameterizing the offset axis into an angle axis to form angle-domain common-image gathers. Unlike ODCIGs, ADCIGs produced with either method have similar characteristics, since they describe the reflectivity as a function of the angle at the reflector.

Depending on the seismic experiment we are analyzing, the coordinates of the image space possess different information relevant to the experiment. We refer to a conventional seismic reflection experiment, where the source and the receiver have the same type of wave, as *single-mode*. For this case, the transformation from ODCIGs to ADCIGs is a well-known process in the literature (Sava and Fomel, 2003). In this case the angle axis represents the true reflection opening angle.

A seismic experiment where the receiver records different components of the wavefield (i.e. P, SV, SH) is known as multi-component seismic; throughout this paper, we refer to the experiment where the source represents a P-wavefield and a receiver wavefield represents a SV-wavefield as a *converted-mode* case, as in the conversion from a P wave into an S wave at the reflection point. This paper discusses the common-image gathers for this kind of experiment, focusing mainly on SODCIGs and their accurate transformation into ADCIGs.

A final side product of our analysis is the ability to separate the final image into two parts, each one corresponding to a distinctive wave. Throughout this process, the ratio between the different velocities plays an important role in the transformation. We present and analyze the kinematics of our equations and present results on two simple yet convincing synthetic examples. An application of our methodology into the 2-D real data set from the Mahogany field in the Gulf of Mexico yields angle-domain common-image gathers that can be used for future velocity updates.

WAVE-EQUATION IMAGING

A prestack image provides information on both velocity errors and rock-property characteristics. This paper obtains the prestack image through wave-equation methods. Several authors have described this process in general, so it will not be the main focus of this paper. However, this section describes the basics of wave-equation imaging, and outlines the method we use to obtain subsurface offset-domain common-image gathers.

Biondi (2003) shows the equivalence of wave-equation source-receiver migration with wave-equation shot-profile migration. The main contribution of this paper is independent of the migration algorithm implemented, as long as the migration algorithm is based on the wavefield downward continuation, and the final prestack image is a function of the horizontal subsurface offset. For the purposes of this paper, we are using shot-profile migration as our imaging algorithm.

The final prestack image is obtained with the following imaging condition (Sava and Fomel, 2005):

$$I(\mathbf{m}_\xi, \mathbf{h}_\xi) = \sum_\omega U_z^s(\mathbf{m}_\xi - \mathbf{h}_\xi, \omega)\overline{U_z^r}(\mathbf{m}_\xi + \mathbf{h}_\xi, \omega). \tag{1}$$

Here, $\mathbf{m}_\xi = (m_\xi, z_\xi)$ is a vector describing the locations of the image points, and $\mathbf{h}_\xi = (h_{x_\xi}, h_{z_\xi})$ is a vector describing the subsurface offset. For 2-D converted-wave seismic data, the component m_ξ represents the horizontal coordinate, z_ξ is the depth coordinate of the image point relative to a reference coordinate system, and h_{x_ξ} is the horizontal subsurface offset (Rickett and Sava, 2002). The summation over temporal frequencies (ω) extracts the image $I(\mathbf{m}_\xi, \mathbf{h}_\xi)$ at zero-time. The propagation of the receiver wavefield (U_z^r) and the source wavefield (U_z^s) is done by downward continuing the recorded data, and the given source wavelet, each one respectively as:

$$\begin{aligned} U_z^s &= U_{z=0}^s e^{+iz\sqrt{\frac{\omega^2}{v_p^2(m_\xi,z_\xi)} - k_{m_{x_\xi}}^2}}, \\ U_z^r &= U_{z=0}^r e^{-iz\sqrt{\frac{\omega^2}{v_s^2(m_\xi,z_\xi)} - k_{m_{x_\xi}}^2}}, \end{aligned} \tag{2}$$

where v_p is the P-wave velocity and v_s is the S-wave velocity.

The next section describes the main focus of this paper, which is the transformation of subsurface offset into the angle domain.

TRANSFORMATION TO THE ANGLE DOMAIN

The transformation to the angle domain follows an approach similar to that of its single-mode (PP) counterpart (Sava and Fomel, 2003). Figure 1 describes the angles we use in this section.

For the converted-mode case, we define the following angles:

$$\begin{aligned} \theta &\equiv \frac{\phi+\sigma}{2}, \\ \alpha &\equiv \frac{2\alpha_x+\phi-\sigma}{2}. \end{aligned} \tag{3}$$

In definition 3 the angles ϕ, σ, and α_x represent the incident, reflected, and geological dip angles, respectively. This definition is consistent with the single-mode case; notice that for the single-mode case the condition that the angles ϕ and σ are the same holds. Therefore, the angle θ represents the reflection angle, and the angle α represents the geological dip (Sava and Fomel, 2003; Biondi and Symes, 2004). For the converted-mode case, the angle θ is the *full-aperture* angle, and the angle α is the *pseudo-geological* dip.

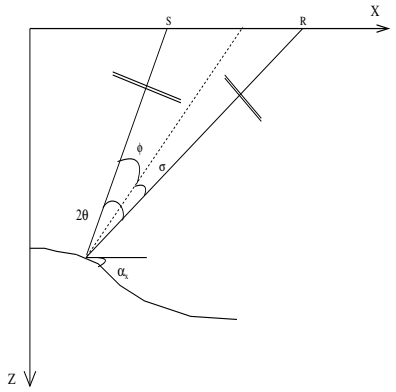

Figure 1: Definition of angles for the converted-mode reflection experiment. The angles θ, ϕ, σ, α_x represent the full-aperture, the incident, the reflection, and the geological dip angles, respectively. daniel1-angles [NR]

The main goal of this paper is to obtain a relationship between the known quantities from our image, $I(\mathbf{m}_\xi, \mathbf{h}_\xi)$ and the *full-aperture* angle (θ). Appendix A presents the full derivation of this relationship. Here, we present only the final result, its explanation and its implications. The final relationship we use to obtain converted-mode angle-domain common-image gathers is the following (Appendix A):

$$\tan\theta = \frac{4\gamma(\mathbf{m}_\xi)\tan\theta_0 + D(\mathbf{m}_\xi)(\gamma(\mathbf{m}_\xi)^2-1)(\tan^2\theta_0+1)}{\tan^2\theta_0(\gamma(\mathbf{m}_\xi)-1)^2+(\gamma(\mathbf{m}_\xi)+1)^2}, \tag{4}$$

this equation consists of three main components: $\gamma(\mathbf{m}_\xi)$ is the P-to-S velocity ratio, $\tan\theta_0$ is the *pseudo-opening* angle, and $D(\mathbf{m}_\xi)$ is the field of local step-outs of the image. Equation 4 describes the transformation from the subsurface-offset domain into the angle domain for converted-wave data. This equation is valid under the assumption of constant velocity. However, it remains valid in a differential sense in an arbitrary-velocity medium, by considering that h_ξ is the subsurface half-offset. Therefore, the limitation of constant velocity applies in the neighborhood of the image. For $\gamma(\mathbf{m}_\xi)$, it is important to consider that every point of the image is related to a point on the velocity model with the same image coordinates.

Transformation into independent angles

Following definition 3, and after explicitly computing the *full-aperture* angle with equation 4, we have almost all the tools to explicitly separate the *full-aperture* angle into its two compo-

nents, the P-incidence angle (ϕ), and the S-reflection angle (σ). Snell's law, and the P-to-S velocity ratio are the final components for this procedure. After basic algebraic and trigonometric manipulations, the final expressions for both of the independent angles are

$$\begin{aligned} \tan\phi &= \frac{\gamma \sin 2\theta}{1+\gamma\cos 2\theta}, \\ \tan\sigma &= \frac{\sin 2\theta}{\gamma+\cos 2\theta}. \end{aligned} \tag{5}$$

This is clearly a non-linear relation among the angles. The main purpose of this set of equations is to observe and analyze the kinematics of the P-incidence wave, and the S-reflected wave. This analysis might lead to estimates of independent velocity perturbations for both the P-velocity model and the S-velocity model. The following section describes the proposed methodology to implement both equation 4 and system 5

Implementation

There are several ways to implement equation 4. The flow in Figure 2 presents the basic steps to implement and obtain the angle-domain common-image gathers for converted-wave data. The first step takes the final image $I(\mathbf{m}_\xi, h_\xi)$ and obtains two main components: first, the intermediate angle gathers, $\tan\theta_0$, using for example, the Fourier-domain approach (Sava and Fomel, 2003); second, the estimated step-out of the image, $D(\mathbf{m}_\xi)$, using plane-wave destructors (Fomel, 2002). This step combines the two previous components, together with the $\gamma(\mathbf{m}_\xi)$-field, and uses equation 4 to form converted-wave angle-domain common-image gathers. The third step divides the PS-ADCIGs into P-ADCIGs and S-ADCIGs. The final step in the diagram flow is responsible for this operation. The following sections present simple

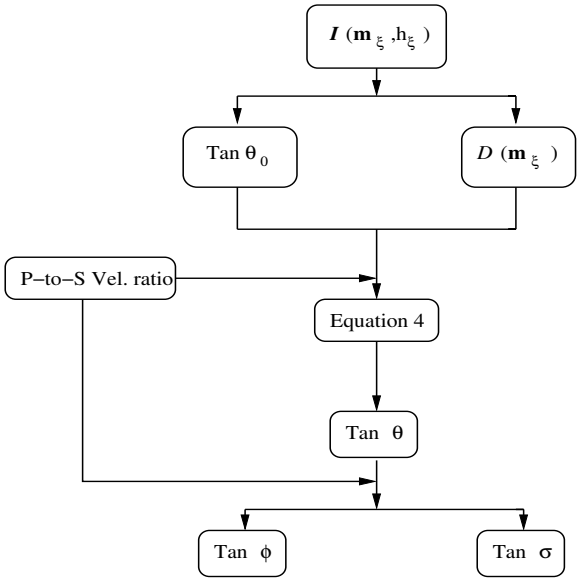

Figure 2: Diagram flow for the subsurface-offset transformation to the angle domain. The flow diagram also presents the computation of the individual P-ADCIGs and S-ADCIGs. daniel1-flow [NR]

synthetic examples as well as a real-data result from the Gulf of Mexico.

Table 1: First synthetic experiment: Acquisition geometry, corresponding computed angle values.

Refl. dip	Shot-loc.	CIG-Loc	$2\theta(^\circ)$
Flat layer	500	2000	40.45°
10° layer	500	1750	38.7°
30° layer	500	1000	35°

SYNTHETIC EXAMPLES

This section consists of two main, simple synthetic examples to illustrate two of the main concepts described in the previous section. Throughout this section, we will refer to two different methodologies, first, the conventional methodology, and second, the proposed methodology. The conventional methodology consists of the transformation from ODCIGs into ADCIGs with the transformation for the single-mode case (Sava and Fomel, 2003). The proposed methodology is the one discussed in the previous section. All the examples are a single-shot gather experiment.

The first example consists of three sections, all of them displayed in Figure 3. From left to right we have a flat-layer, a 10° dipping layer, and a 30° dipping layer. All the sections consist of, from top to bottom, a single shot gather, an image from one shot gather, an angle-domain common-image gather obtained with the conventional methodology, and the angle-domain common-image gather obtained with the proposed methodology. The data space consists of only one shot gather; therefore, the representation in an ADCIG should have non-zero energy for only one angle. Table 1 shows the survey details and the computed angle values for this experiment. In both angle-domain gathers, the solid line corresponds to the expected angle value; as expected the angle gathers obtained with the proposed methodology perfectly match the values in the table.

Our second experiment is also a single-shot experiment. The intention of this exercise is to present the separation of the *full-aperture* angle (θ) into its P-incidence (ϕ), and its S-reflection (σ) components. Figure 4 shows, from top to bottom, the flat-layer case, a 10° dipping layer case, and a 30° dipping layer case for this experiment. Each case consists of, from left to right, the image of a single-shot gather; the corresponding angle-domain common-image gather, which is taken at the location marked in the image; the corresponding P-angle-domain common-image gather; and the corresponding S-angle-domain common-image gather. Table 2 shows the corresponding values for this experiment. The solid lines in each of the angle-gathers represent the computed value in table 2.

These two synthetic examples clearly show that the proposed methodology accurately transforms SODCIGs into ADCIGs for the converted-mode case. Moreover, we are able to compute the specific incidence and reflection angles.

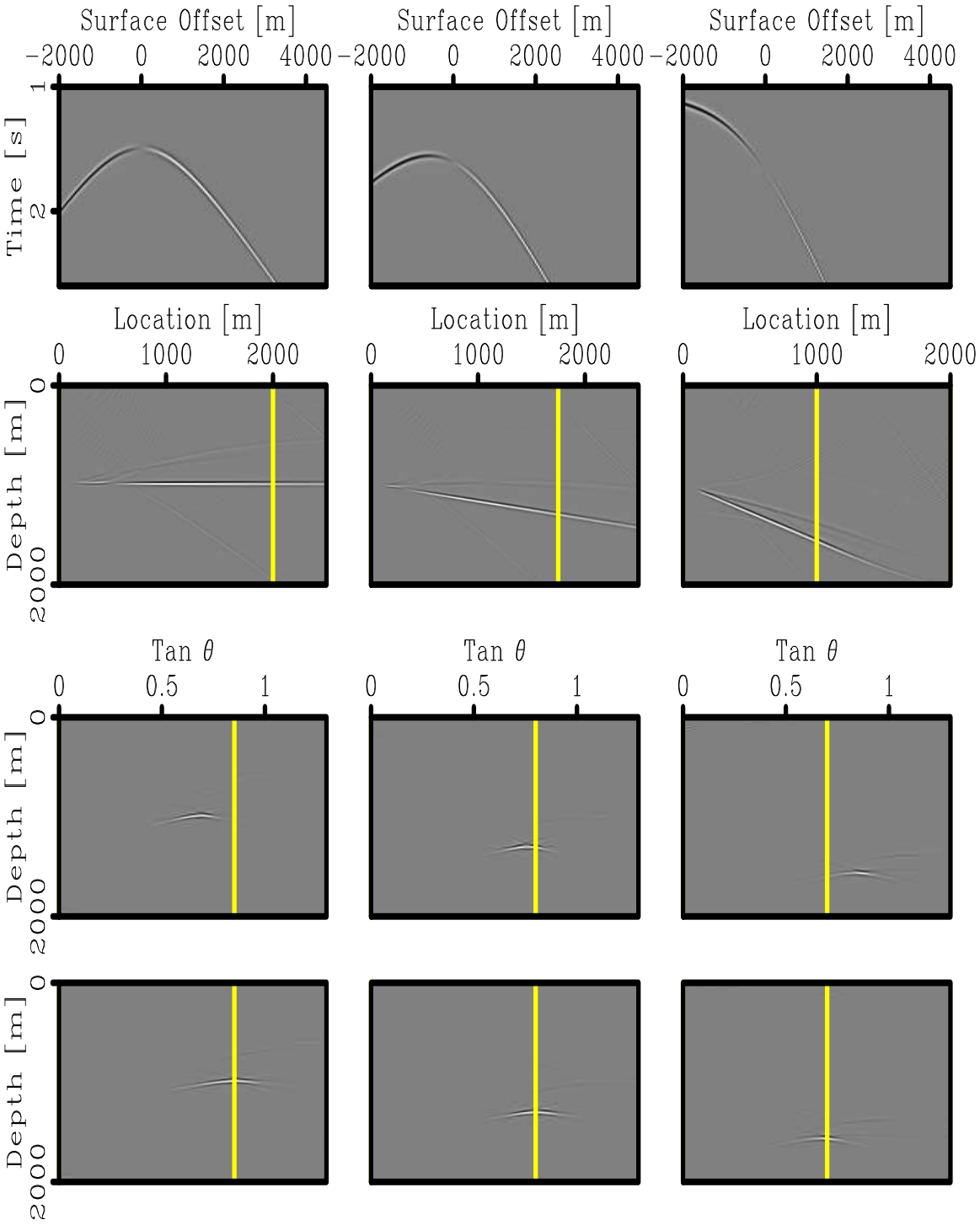

Figure 3: First synthetic example. From left to right, a flat-layer case, a 10° dipping layer, and a 30° dipping layer. From top to bottom, a single shot gather, an image from a single shot gather, an angle-domain common-image gather obtained with the conventional methodology, and the angle-domain common-image gather obtained with the proposed methodology. daniel1-ps-all-x [CR]

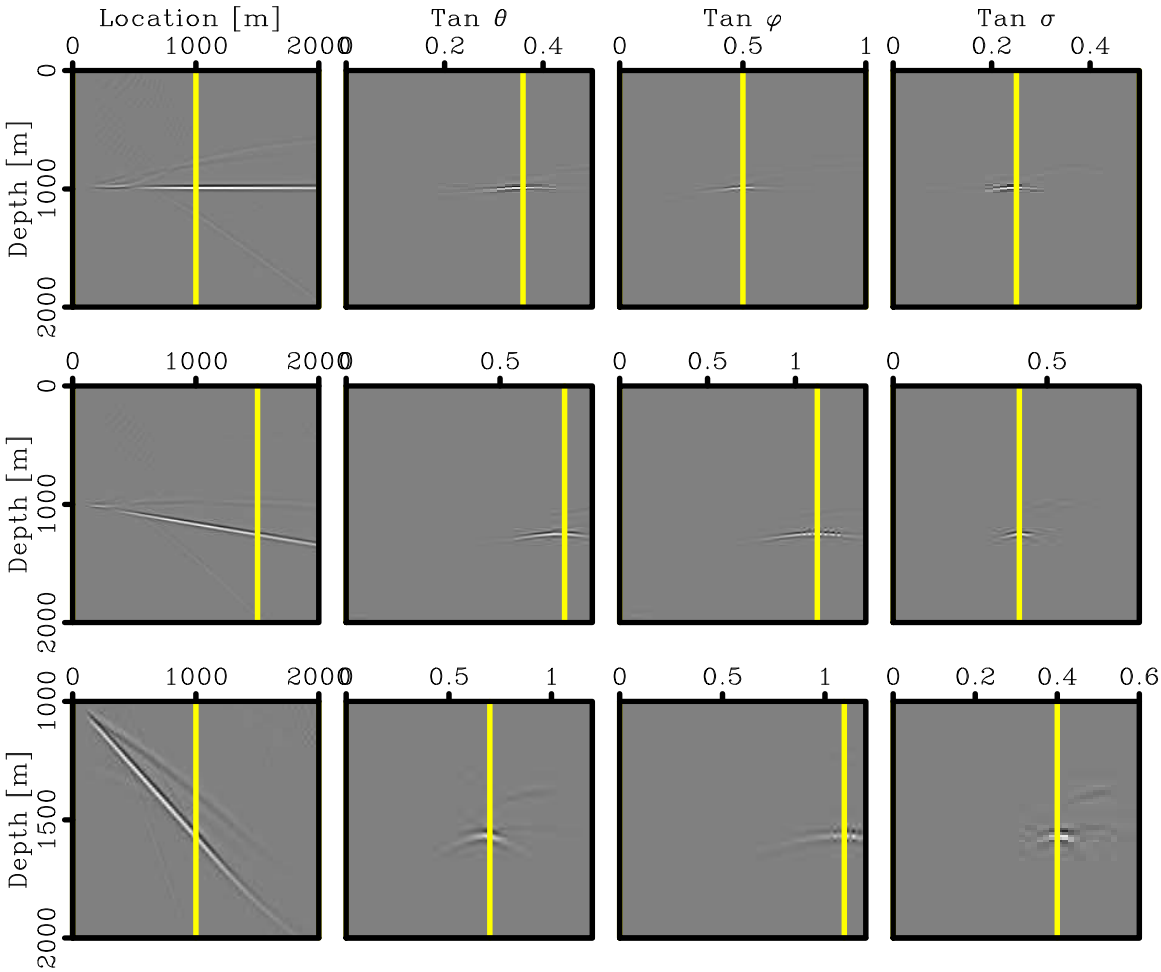

Figure 4: Second synthetic example, independent angle separation: From top to bottom, a flat-layer case, a 10° dipping layer, and a 30° dipping layer. From left to right: the image of a single shot gather, the corresponding PS-ADCIG, the independent P-ADCIG, and the independent S-ADCIG. The solid lanes represent the corresponding values in table 2. daniel1-ps-ind-ang [CR]

REAL DATA EXAMPLE

This test uses a portion of the 2-D real data set from the Mahogany field, located in the Gulf of Mexico. The 2-D data set is an Ocean Bottom Seismic (OBS) multicomponent line. The data has been already preprocessed. The hydrophone and the vertical components of the geophone has been combined to form the PZ section. Also, the data has also been separated into the PS section. We concentrate on the PZ section and the PS section.

Figure 5 presents a typical shot gather for this OBS data set. On the left we have the PZ common-shot gather, and on the right we have the PS common-shot gather. The PZ shot gather has fewer time samples than the PS shot gather because of the longer time needed to observe the converted-wave events. Also, note the polarity flip in the PS common-shot gather, a typical

Table 2: Second synthetic experiment: Acquisition geometry, corresponding computed angle values.

Refl. dip	Shot-loc.	CIG-Loc.	P-angle	S-angle
Flat layer	500	1000	26°	14°
10° layer	500	1500	48°	22.3°
30° layer	500	1000	47°	22°

characteristic of this type of data set.

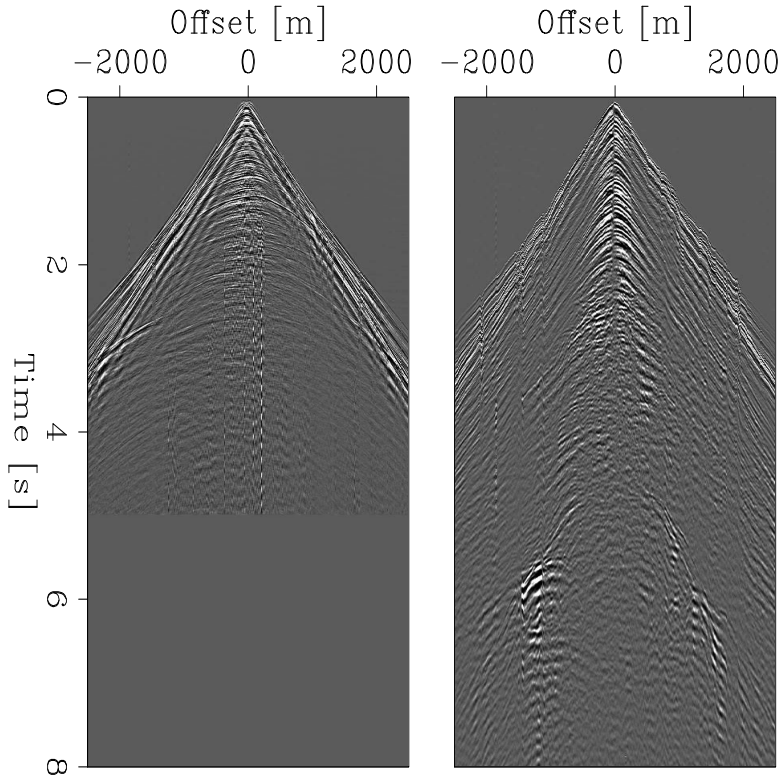

Figure 5: Typical common-shot gathers for the OBS Mahogany data set from the Gulf of Mexico. Shot gather after PZ summation (a), PS shot gather (b). daniel1-shots [CR]

In both data sets, the PZ and the PS components were migrated using wave-equation shot-profile migration. Both, the P and the S velocity models are unknown for this problem; for simplicity, migrate using a velocity model with a linear gradient, Figure 6 shows both velocity models, the P-velocity model on the left panel, and the S-velocity model in the right panel. Complementary, Figure 7 represents the local step-out field for this experiment.

Figure 8 presents a PS image on the left, and two angle-domain common-image gathers on the right. Both common-image gathers are taken at the same location, indicated by the solid

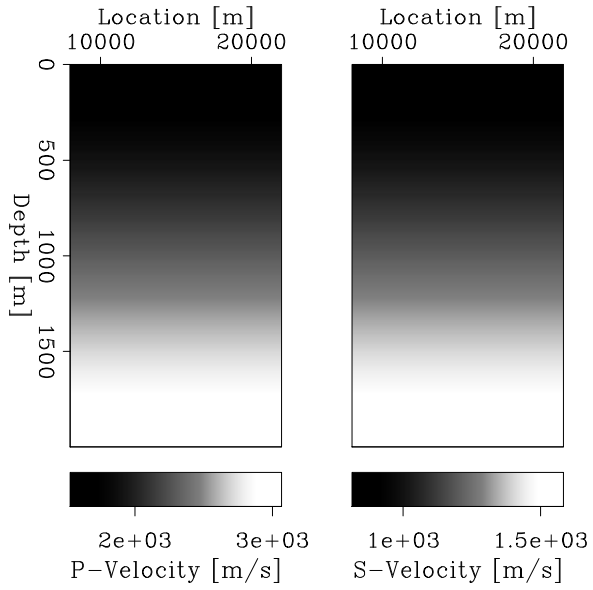

Figure 6: Velocity models used for the shot-gather migration. P-velocity on the left panel, S-velocity on the right panel. daniel1-vels [CR]

line at CIG=14500 in the image. The PS image was taken at zero subsurface offset, this is not the ideal position to take the final image, since the polarity flip destroys the image at this location. The ideal case will be flip the polarities in the angle domain (Rosales and Rickett, 2001); unfortunately, we do not have the correct velocity model yet; therefore, we have only an approximate solution to the final PS image.

The angle-domain common-image gather on panel (b) of Figure 8 represents the angle-domain common-image gathers using the conventional methodology, which will be $\tan\theta_0$ on the diagram flow on Figure 2. The angle-domain common-image gather on panel (c), represents the true converted-wave angle-domain common-image gather. The transformation to the angle-domain was performed with the diagram flow on Figure 2.

The geology for this section of the Mahogany data set consists of very low geological dips, with a relatively layering; therefore, the angle gather on panel (b) has the polarity flip very close to zero angle. The true angle gather also preserves this characteristic. The residual curvature for the events, whether primaries or multiples, is much larger than the residual curvature of the same events in the true angle-domain common-image gather. This effect is due to the correction for both the step-out of the image and the P-to-S velocity ratio, as presented in the theory section of this paper.

Figure 9 presents the PS and the PZ results of shot-profile migration with the velocity models on Figure 6. Panel (a) presents the PS image on the top and its corresponding angle-domain common-image gathers on the bottom. Panel (b) presents the PZ image on the top and its corresponding angle-domain common-image gathers on the bottom. In both representations of the angle gathers, it is possible to observe events at a very similar depth, these events probably represent the same geological feature. Also notice the many multiples, due to the shallow sea bottom (120 m). These multiples are more prominent in the PS section because the PZ summation already eliminates the source ghost. This is not the case for the PS section.

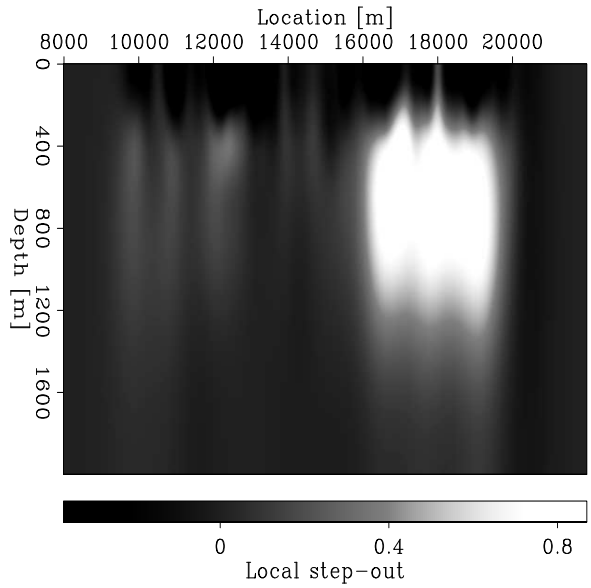

Figure 7: Local step-out of the image; this represents the field $D(\mathbf{m}_\xi)$ on equation 4. daniel1-dips [CR]

Figure 10 compiles all the different angle-domain common-image gathers for this data set, all of which are taken at the same position, CIG=14500. From left to right, the panels show PP-ADCIG, PS-ADCIG, P-ADCIG, and S-ADCIG. Notice that most of the primary events have a residual curvature. The residual moveout is more prominent for those events that we identify as multiples.

The initial linear P-velocity model is a pretty good approximation, since most of the primary events in the PZ section are flat in the angle-domain. However, there is a prominent residual curvature in the angle-domain common-image gathers for the PS section. This indicates an erroneous velocity model, most likely a very high initial S-velocity model. Moreover, the S section contains a large number of multiples, which are not all present in the PZ section.

The individuals P-ADCIG and the S-ADCIG contain information that potentially can be used for independent velocity updates. Notice that the angle coverage for these gathers is smaller than for the PP- and-PS ADCIGs, since the coverage of an individual plane-wave is smaller than the combination of two plane-waves, as is the case for converted-mode data.

It is very interesting to notice that the individual P-ADCIG has very similar characteristics with the PP-ADCIG. Most of the residual moveout of the PS-ADCIG seems to be due to the S component of the velocity model, as suggested for the individual S-ADCIG.

CONCLUSIONS

The accurate transformation from subsurface offset-domain CIGs into angle-domain CIGs for the converted-mode case requires, the information along the midpoint axis, and the velocity ratio. Omitting this information leads to errors in the transformation that might result in incorrect velocity updates.

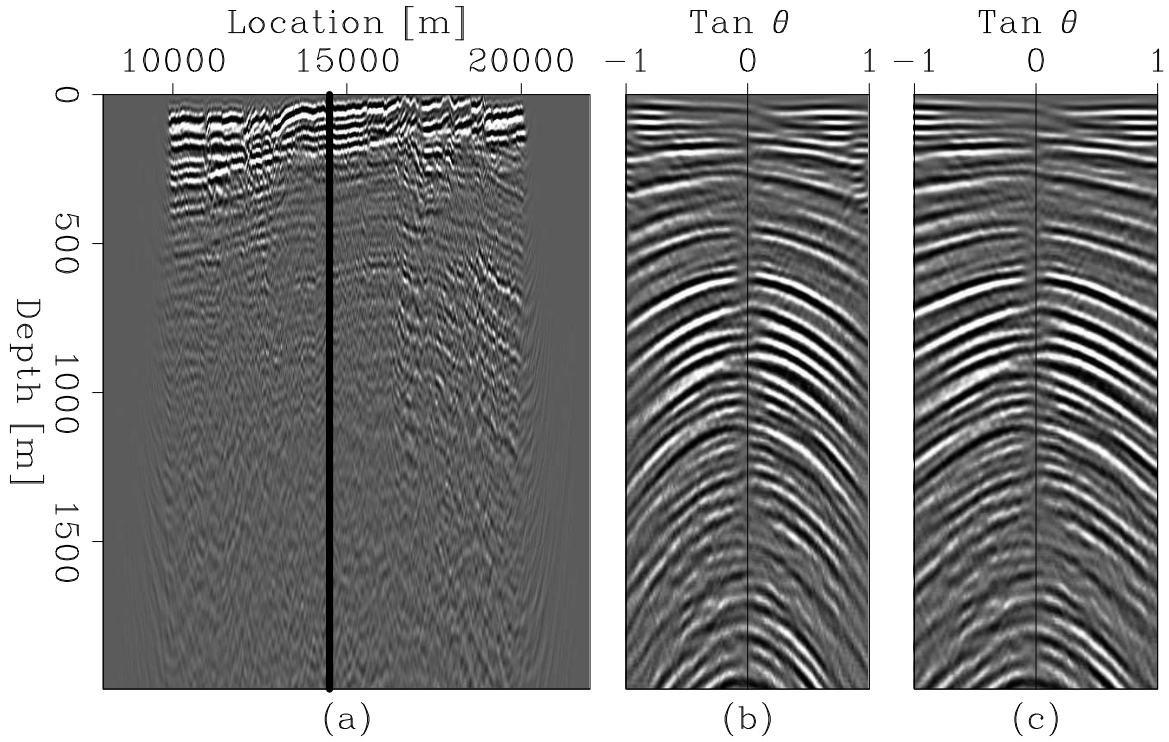

Figure 8: PS image on the left, and two angle-domain common-image gathers on the right; both common-image gathers are taken at the same location, as represented by the solid line at CIG=14500 in the image. daniel1-psimg-adcig [CR]

For the converted-mode case, the angle axis of the final image ($I(\mathbf{m}_\xi, \gamma)$), after the transformation, is neither the incidence nor the reflection angle, but the average of both. The *full-aperture* angle gathers can be transformed into two separate angle gathers, each one representing the incidence angle and the other representing the reflection angle. This transformation might yield useful information for the analysis of rock properties or velocity updates for the two different velocity models.

The next step will be to analyze how errors in either P or S velocity models are transformed in the PS-ADCIGs. This will result in both a formulation for the residual moveout of converted-mode data, and a methodology for vertical velocity updates of both P and S velocity models.

ACKNOWLEDGMENTS

We would like to thank CGG for providing the data used in this paper.

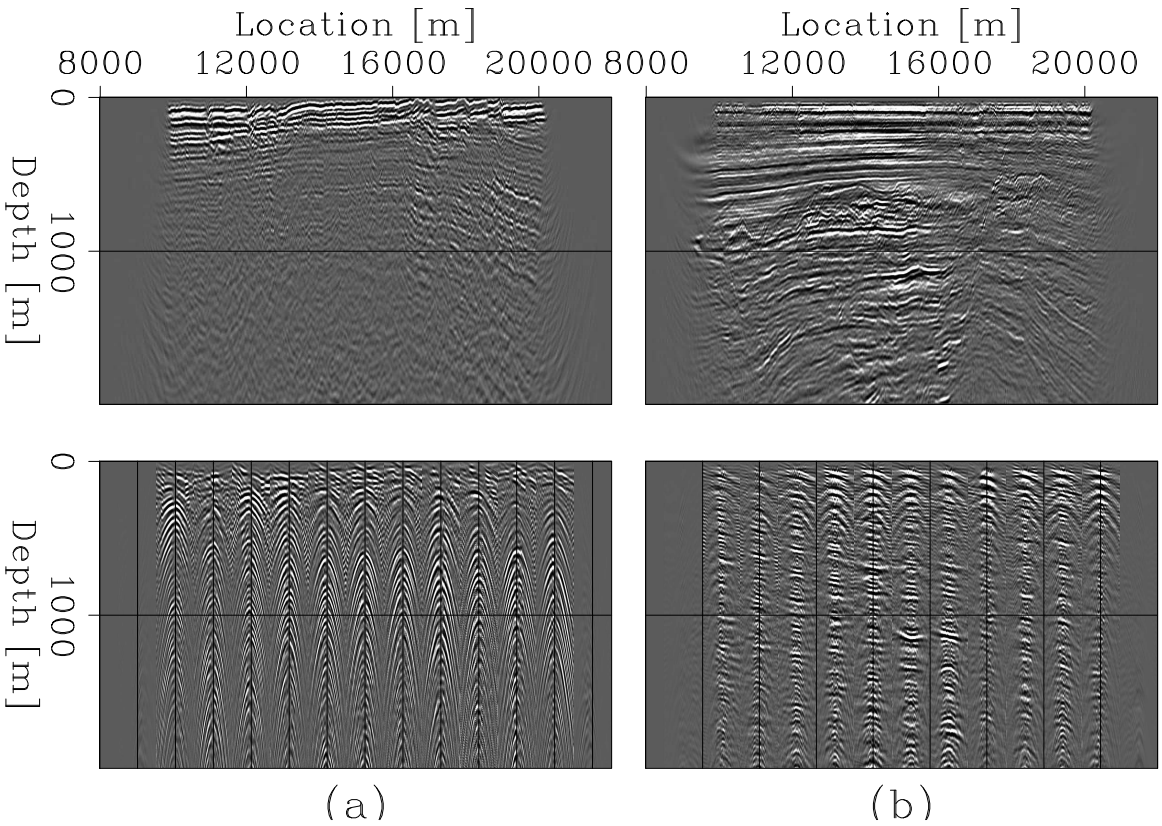

Figure 9: Panel (a) presents the PS image with its respective angle-domain common-image gathers. Panel (b) presents the PZ image with its respective angle-domain common-image gathers. daniel1-imag-cigs [CR]

APPENDIX A

DERIVATION OF THE EQUATION FOR THE ANGLE-DOMAIN TRANSFORMATION

This appendix presents the derivation of the main equation for this paper, that is, the transformation from the subsurface offset domain into the angle domain for converted-wave data. Rosales and Biondi (2005) present the derivation for the angle-domain transformation. Biondi (2005) and Shragge et al. (2005) present similar equations for different applications, for anisotropic case and for the forward-scatter case, respectively. Throughout this Appendix we will use the following defintions:

$$\begin{aligned} \tan\theta_0 &\equiv -\frac{\partial z_\xi}{\partial h_\xi} \\ D(\mathbf{m}_\xi) &\equiv -\frac{\partial z_\xi}{\partial m_\xi} \end{aligned}$$

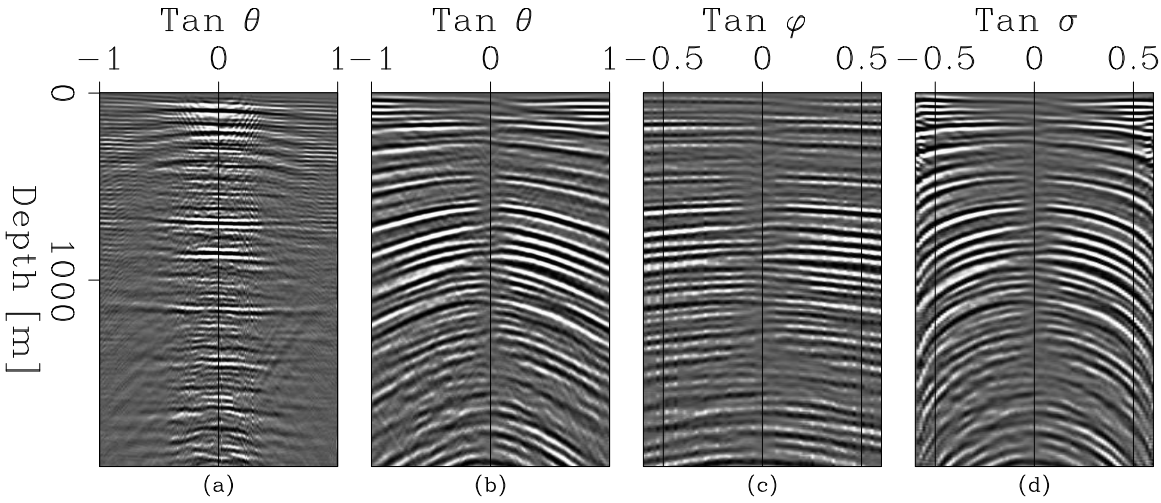

Figure 10: Compilation of angle-domain common-image gather for the 2-D Mahogany data set, all the CIGs are taken at the same image location (CIG=14500). (a) PP-ADCIG, (b) PS-ADCIG, (c) P-ADCIG, (d) S-ADCIG. daniel1-cigs-all [CR]

In this definitions, $\tan\theta_0$ is the *pseudo-reflection* angle, and $D(\mathbf{m}_\xi)$ is field for the local image dips. The bases for this definition resides in the conventional PP case. For that case, the *pseudo-reflection* angle represents the reflection angle, and the field $D(\mathbf{m}_\xi)$ represents the geological dip (Fomel, 1996). Based on this definition, the angle equations from Biondi (2005); Rosales and Biondi (2005); Shragge et al. (2005) can be rewritten as:

$$\tan\theta_0 = \frac{\tan\theta + \mathscr{S}\tan\alpha}{1 - \mathscr{S}\tan\alpha\tan\gamma}, \tag{A-1}$$

$$D(\mathbf{m}_\xi) = \frac{\tan\alpha + \mathscr{S}\tan\theta}{1 - \mathscr{S}\tan\theta\tan\alpha.} \tag{A-2}$$

Following basic algebra, equation A-2 can be rewritten as:

$$\tan\alpha = \frac{D(\mathbf{m}_\xi) - \mathscr{S}\tan\theta}{1 - \mathscr{S}D(\mathbf{m}_\xi)\tan\theta} \tag{A-3}$$

Substituing equation A-3 into equation A-1, and following basic algebraic manipulations, we obtain equation 4 in the paper.

REFERENCES

Biondi, B. and W. Symes, 2004, Angle-domain common-image gathers for migration velocity analysis by wavefield-continuation imaging: Geophysics, **69**, no. 5, 1283–1298.

Biondi, B., 2003, Equivalence of source-receiver migration and shot-profile migration: Equivalence of source-receiver migration and shot-profile migration:, Soc. of Expl. Geophys., Geophysics, 1340–1347.

Biondi, B., 2005, Angle-domain common image gathers for anisotropic migration: SEP–**120**, 77–104.

Brandsberg-Dahl, S., M. V. de Hoop, and B. Ursin, 1999, The sensitivity transform in the common scattering-angle/azimuth domain: 61st Ann. Internat. Mtg., Soc. Expl. Geophys., Expanded Abstracts, 1538–1541.

de Bruin, C. G. M., C. P. A. Wapenaar, and A. J. Berkhout, 1990, Angle-dependent reflectivity by means of prestack migration: Geophysics, **55**, no. 9, 1223–1234.

Fomel, S., 1996, Migration and velocity analysis by velocity continuation: SEP–**92**, 159–188.

Fomel, S., 2002, Applications of plane-wave destruction filters: Geophysics, **67**, no. 6, 1946–1960.

Prucha, M., B. Biondi, and W. Symes, 1999, Angle-domain common-image gathers by wave-equation migration: 69th Ann. Internat. Meeting, Soc. of Expl. Geophys., Expanded Abstracts, 824–827.

Rickett, J. and P. Sava, 2002, Offset and angle-domain common image-point gathers for shot-profile migration: Geophysics, **67**, 883–889.

Rosales, D. A. and B. Biondi, 2005, Converted-mode angle-domain common-image gathers for migration velocity analysis: SEP–**120**, 283–296.

Rosales, D. and J. Rickett, 2001, PS-wave polarity reversal in angle domain common-image gathers: 71st Annual Internat. Mtg., Expanded Abstracts, 1843–1846.

Sava, P. and S. Fomel, 2003, Angle-domain common-image gathers by wavefield continuation methods: Geophysics, **68**, no. 3, 1065–1074.

Sava, P. and S. Fomel, 2005, Coordinate-independent angle-gathers for wave equation migration: 75th Annual Internat. Mtg., Expanded Abstracts.

Shragge, J., B. Artman, and B. Biondi, 2005, Adcigs for forward-scattered wavefields: SEP–**120**, 257–270.